45 W average-power, high-energy deep-UV generation at 257 nm in LBO

Gabriel Mennerat, Laurent Bizet, Benoît Mahieu, Alexandre Dobroc, Dominique Lupinski, Denis Balitsky, Philippe Villeval, Magali Lozano, Fatima Alahyane, Aurélien Houard, et al.

45 W average-power, high-energy deep-UV generation at 257 nm in LBO

Gabriel Mennerat[a], Laurent Bizet[b], Benoît Mahieu[b], Alexandre Dobroc[c], Dominique Lupinski[c], Denis Balitsky[c], Philippe Villeval[c], Magali Lozano[b], Fatima Alahyane[b], Aurélien Houard[b], Jean-Pierre Wolf[d]

[a]Université Paris-Saclay, CEA, LIDYL, 91191 Gif-sur-Yvette, France
[b]Laboratoire d'Optique Appliquée – ENSTA Paris, École Polytechnique, CNRS, IP Paris, 91762 Palaiseau, France
[c]Cristal Laser, 54850 Messein, France
[d]Groupe de Physique Appliquée, Université de Genève, Geneva, Switzerland

ABSTRACT

We report on high average-power, high-energy picosecond fourth-harmonic generation in LBO. The first stages of a Yb:YAG laser chain operating at 1 kHz repetition rate generate few-picosecond 220 mJ chirped pulses at 1030 nm fundamental wavelength. They are frequency-converted in a cascade of three LBO crystals to generate the second-, third-, and fourth-harmonics at 515 nm, 343 nm and 257 nm respectively. Crystals thicknesses and angular phase-matching detuning were calculated as a function of pulse duration through broadband nonlinear optical numerical simulations. Last crystal is both conduction-cooled on edge and surface-cooled at center through forced-air flow to mitigate heating due to nonlinear absorption in the deep-UV and reduce temperature gradients. Chirped-pulse duration was experimentally adjusted to achieve stable 20% overall conversion efficiency. Near-field beam profiles were continuously recorded at 10 Hz, for all four wavelengths involved, together with corresponding energies, showing no significant beam degradation over 50 hours. Temperatures of the two last crystals were monitored, and will help optimize surface cooling for future power ramping-up.

Keywords: visible-UV generation, new concepts of nonlinear optics

1. INTRODUCTION

Frequency-doubled and frequency–tripled near-infrared solid-state lasers almost totally replaced continuous-wave and pulsed ion, gas, and excimer lasers lasers (argon copper-vapor, nitrogen) two decades ago for wavelengths above 350 nm in the green and near ultraviolet. A number of important applications in the semiconductor industry, manufacturing, and science, require high-power lasers at shorter wavelengths, below 300 nm. For lightning control applications,[1] wavelengths even shorter than the third-harmonic[2] of the near-infrared fundamental radiation could be more advantageous, as ionisation of the air molecules would require even less photons.

High-average power all-solid-state frequency-conversion to the deep-ultraviolet faces significant and enduring challenges:

1. limited choice of mature transparent materials with suitable thermal properties;
2. limited choice of phase-matchable birefringent crystals;
3. strong multi-photon non-linear absorption, and strong optical Kerr effet, since the generated-photons energies are close to electronic band-gap;
4. surface contamination and bulk-material aging.

Further author information: (Send correspondence to Gabriel Mennerat)
G. Mennerat: E-mail: gabriel.mennerat@cea.fr, Telephone: +33 1 69 08 59 61

Nonlinear Frequency Generation and Conversion: Materials and Devices XXIII,
edited by Peter G. Schunemann, Proc. of SPIE Vol. 12869, 128690I
 · 0277-786X · doi: 10.1117/12.3001107

Lithium triborate LiB_3O_5 (LBO) is a mature, homogeneous, and optical-damage resistant material, now available in large dimensions,[3] and capable of generating hundreds of Joules[4,5] in the green (527 nm) and near-ultraviolet (351 nm) with outstanding conversion efficiencies above 92% and 85% respectively. Phase-matched frequency conversion to deeper ultraviolet requires a stronger optical birefringence to compensate for increased chromatic dispersion at shorter wavelengths. Birefringence is smaller in LBO than in most other deep-UV non-linear optical crystals like KDP,[6] β-BBO,[7] or CLBO.[8] This precludes direct frequency doubling from the green to the 250-270 nm ultraviolet wavelength range. Three-stage sum-frequency conversion is necessary and was already demonstrated as an efficient path for multiwatt generation (up to 7 W)[9] to the deep-UV in the nanosecond regime, as well as high-energy sub-nanosecond[10] pulse durations.

We demonstrate here a novel cooling strategy, that mitigates thermal drifting induced by residual linear and deeper-ultraviolet nonlinear absorption in large area crystals at high-energy, in the much more intense picosecond regime. This permits to reproducibly generate stable world-record average power above 40 W in the deep-UV, and produce clean beams that would be usable for long-distance filamentation applications.[11,12] This also makes it possible to address other limiting phenomena and make progress towards efficient and reliable industrial systems.

2. DESIGN AND SIMULATION OF THE FREQUENCY CONVERSION CHAIN

Pristine spare doubler (SHG) and tripler (THG) crystals manufactured for previous experiments[2] were employed as the two first frequency-conversion stages. The thickness of the quadrupler crystal to be cut and polished for this experiment was specified according to numerical simulations of the three-stage setup depicted in figure 1.

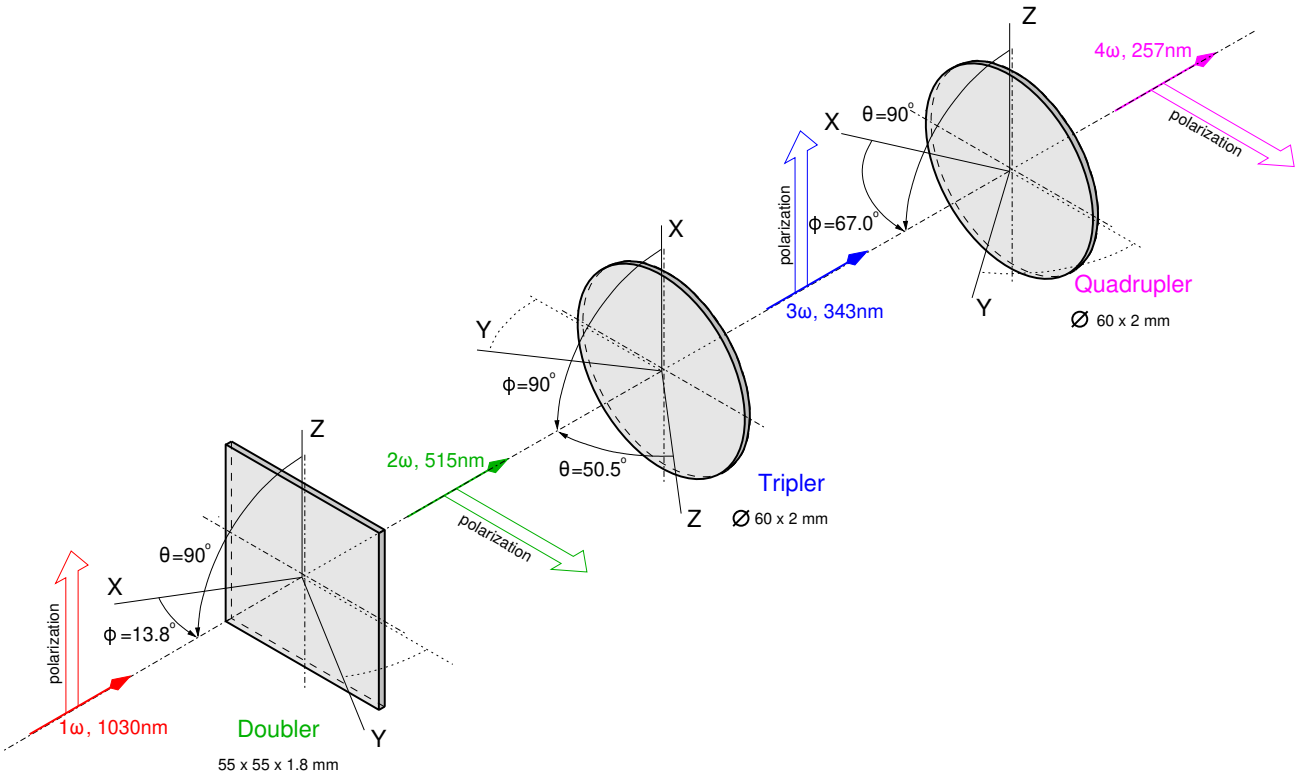

Figure 1. Orientation and dimensions of the three LBO crystals in series for frequency quadrupling

2.1 Optimisation of Quadrupler Thickness for 500 mJ Input Energy

The broadband spatio-temporal frequency-conversion model[13,14] used to simulate the frequency conversion chain is similar to the 2D-mix-SP module of the SNLO[15] code. In addition to air-space dispersive linear propagation between converters to provide electric fields from previous stage at input of each stage, it includes a number

of sophistications like arbitrary multiple three-wave $\chi^{(2)}$ and four-wave $\chi^{(3)}$ mixing interactions, full anisotropy permitting propagation out-of-principal planes, full chromatic dispersion of the principal refractive indices[16] allowing for broader-wave and shorter-pulse calculations, and inclusion of thermally-induced effects thanks to calls to finite-element calculations fully integrated within the adaptive step-size split-step integration algorithm. It will be described in a forthcoming paper. Anisotropic and dispersive direct $\chi^{(3)}$ optical Kerr effect was included in the model in addition to cascaded $\chi^{(2)} : \chi^{(2)}$ effect for the determination of crystal thickness. Miller scaling was tentatively applied to quadratic[17,18,19] and cubic[20] nonlinear optical coefficients (see table 1). Kerr coefficients are unknown. At present we base Miller scaling on the reported value of $2.2 \times 10^{-20}\,\mathrm{m^2/W}$ for self-phase modulation[21,22] at 266 nm. This value corresponds neither to the actual polarisation of the 4ω wave nor to the quadrupler crystal orientation.

Multi-photon absorption[23,24] and the effects of associated induced thermal loading were neglected for a number of reasons. First, direct energy attenuation due to nonlinear absorption is small compared to other factors investigated here. Second, the effects of crystal heating on frequency conversion - namely temperature gradients, and phase-matching detuning - are significant but they are expected to be eventually mitigated through our surface cooling technique. Lastly, none of the coefficients for cross-multi photon absorption of any order could be realistically guessed in the deep-UV at this stage. Crystals are therefore fully anisotropic as far as their linear, quadratic, and cubic nonlinear optical properties are concerned but they do not heat up. They are therefore spatially homogeneous.

Table 1. Material parameters for simulation of the three frequency-conversion crystals, including tentative Kerr coefficients γ_{ij} for self- $(i = j)$ and cross- $(i \neq j)$ phase modulation.

	doubler	**tripler**	**quadrupler**
cut-angles $(\theta;\varphi)$	$(90;13.6)^o$	$(50.5;90)^o$	$(90;66.5)^o$
spatial walk-off angle ρ	8.2 mrad	9.2 mrad	15.1 mrad
group velocity indices	1.626 ; 1.626 ; 1.642	1.582 ; 1.653 ; 1.674	1.626 ; 1.731 ; 1.791
effective nonlinear coefficient d_{eff}	0.828 pm/V	0.465 pm/V	0.388 pm/V
Kerr coefficients $\gamma_{ij} \times 10^{-20}\,\mathbf{m^2/W}$	γ_{11}=2.2 ; γ_{22}=2.42	γ_{11}=2.17 ; γ_{22}=2.46	γ_{11}=2.2 ; γ_{22}=2.42
Miller-scaling (tentative)	$\gamma_{12}=\gamma_{21}$=1.54	$\gamma_{12}=\gamma_{21}$=1.54	$\gamma_{12}=\gamma_{21}$=1.54
		$\gamma_{13}=\gamma_{31}$=4.96	$\gamma_{13}=\gamma_{31}$=5.02
		$\gamma_{23}=\gamma_{32}$=1.76	$\gamma_{23}=\gamma_{32}$=1.76
		γ_{33}=2.83	γ_{33}=2.87 ; γ_{44}=3.53
			$\gamma_{14}=\gamma_{41}$=1.85
			$\gamma_{24}=\gamma_{42}$=5.85
			$\gamma_{34}=\gamma_{43}$=2.12

We assumed a transform-limited 1 ps Gaussian input pulse at 1030 nm central wavelength with a Gaussian $\mathrm{TEM_{00}}$ spatial shape characterised by a 26 mm $1/e^2$ diameter. Input energy of 500 mJ typical of the laser system was considered. In these conditions input peak fluence is slightly below $0.19\,\mathrm{J/cm^2}$, which is rather conservative. The input pulse duration was numerically stretched to various durations from 1 ps (full-width half-maximum, maximum compression) to 15 ps with either positive or negative ϕ_2, while keeping both its 1.56 nm FWHM bandwidth and energy constant. Corresponding peak intensities vary from $188\,\mathrm{GW/cm^2}$ at maximum compression to $12.5\,\mathrm{GW/cm^2}$ for a 15 ps duration.

The quadrupler thickness was varied from 1 mm to 3 mm. The results of these simulations are plotted in fig. 2. It was found that a 2 mm thickness, and a 6 ps pulse duration are theoretically optimal, and would in this best case produce up to 185 mJ at 257 nm out of 500 mJ at 1030 nm. This maximum theoretical energy conversion efficiency of 37% is clearly limited by the sum-frequency mixing bandwidth of the quadrupler. Due to group velocity mismatch, pulses at 3ω lag behind pulses at 1ω as they propagate through the quadrupler. Components at sum-frequencies around 4ω are even further delayed, resulting in growing three-wave mixing phase-mismatch, eventually leading to back-conversion after some distance. According to simulations, this bandwidth limitation does not substantially reduce fourth-harmonic energy compared to monochromatic pulses of similar peak intensity

in a 2 mm-thick quadrupler. But it precludes thicker quadrupler crystals that further enhance efficiency with artificial monochromatic waves. Maximum theoretical conversion efficiency drops to 29% (147 mJ) in 3 mm-thick crystals with our broadband model but raises up to 51% (253 mJ) with a monochromatic model.

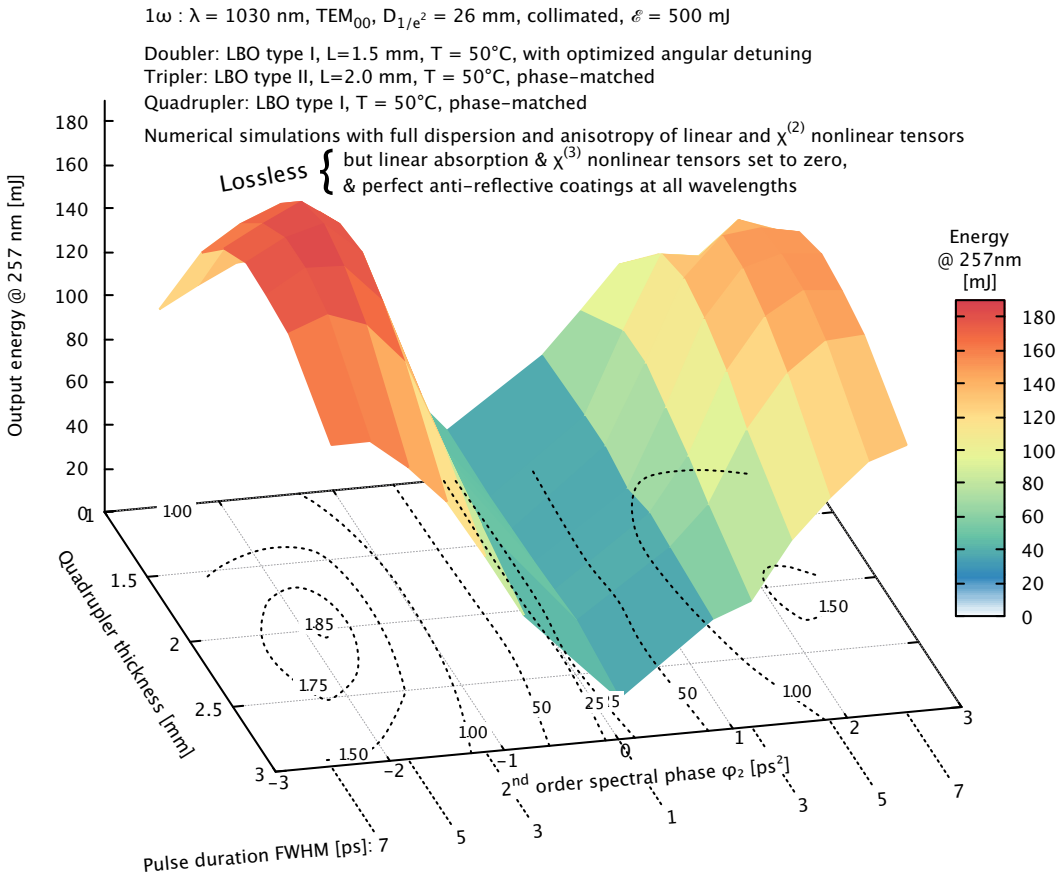

Figure 2. Numerical simulations of generated fourth-harmonic energy at 257 nm

2.2 Expected Performance vs Input Energy

Optimum frequency mixing in the quadrupler requires a 3-to-1 ratio in intensity at input between the wave at 3ω generated in the tripler, and the depleted wave at 1ω emerging from it. Since input intensity at 1ω on the doubler varies in space (TEM_{00}) and time (Gaussian pulse) it is impossible to achieve this ratio over the full beam and during the whole pulse. As analysed in[25] angular detuning of the doubler is sufficient to optimize photon-balance at the quadrupler input in order to maximize the generated energy at 4ω. Multi-variable numerical optimisation, tuning all three crystals angles and pulse stretching, shows that this conclusion drawn for monochromatic waves is still valid for broadband 1 ps pulses and for thicknesses considered here. Optimum energy performance and corresponding parameters are plotted in fig. 3 for our stack of three 1.8 mm-, 2 mm-, and 2 mm-crystals as a function of input pulse energy, up to 800 mJ. With our given 1.8 mm-thick doubler, the optimum angular detuning in the critical XY principal optical plane is of the order of 10 mrad for input energies above 200 mJ.

At very low input energy, maximum pulse recompression down to 1 ps duration (red) and perfect phase-matching in the doubler is required to compensate for inefficient low-intensity frequency conversion. As energy increases up to 50 mJ, detuning the doubler (green) helps moderate stronger and stronger depletion at 1ω at the peak of the input intensity distribution, so that enough infrared radiation remains at quadrupler input.

Stretching input pulse from 1 ps to 1.5 ps contributes. Phase mismatch due to angular detuning induces Kerr-like phase-modulation through $\chi^{(2)} : \chi^{(2)}$ cascading, that compounds with direct $\chi^{(3)}$ Kerr effect. Omitting $\chi^{(3)}$ Kerr effect shifts the optimum detuning angle (dashed lines) in the 50 mJ to 200 mJ input energy range and would require further analysis when actual Kerr coefficients are known.

Conversion efficiency (violet) saturates for input energies between 100 mJ and 200 mJ. Optimum angular detuning is constant for input energies above 200 mJ and the increase of input energy can just be compensated for by a proportional increase of stretched pulse duration. Output energy at 257 nm increases linearly as well , up to 275 mJ for the 800 mJ maximum energy delivered by the laser system.

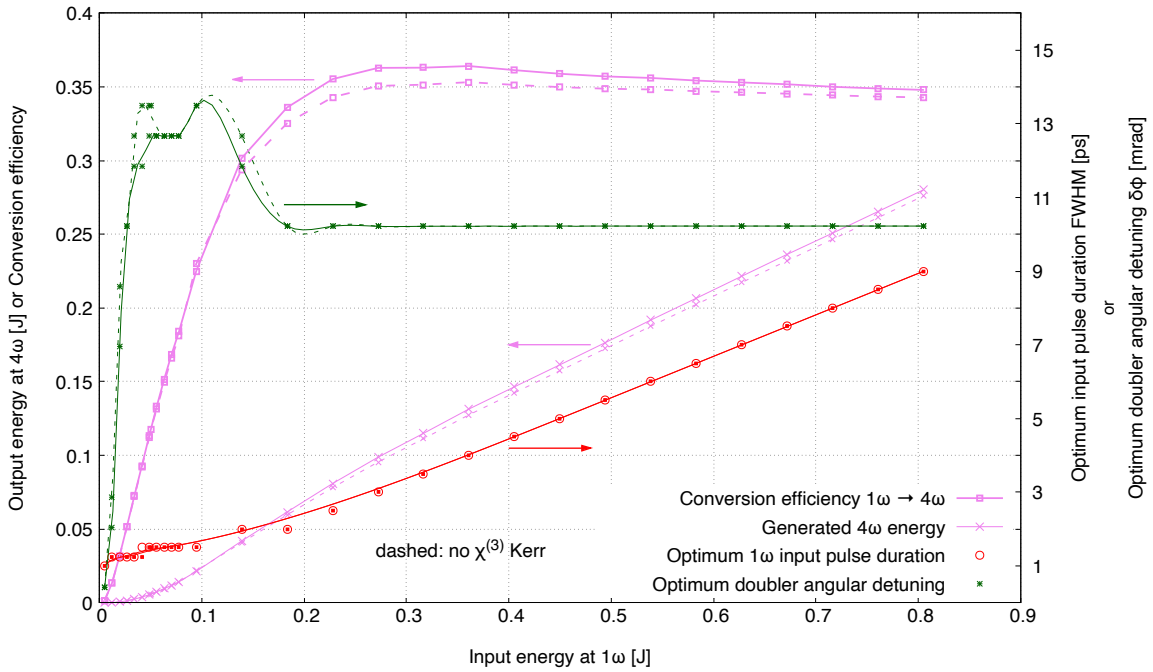

Figure 3. Numerical simulations of optimum parameter over the full energy range of the laser system

3. THERMAL MANAGEMENT

Physical mechanisms limiting the average power in nonlinear frequency converters differ considerably from those occuring in active laser media. Although the thermal load in nonlinear crystals is usually weaker, temperature sensitivity is much higher. In solid-state laser amplifiers, pump-energy is deposited in the volume of the laser medium and most of it is extracted through laser amplification. However, a substantial fraction (10 to 30%) of this energy is wasted as heat in the volume of the material. As a consequence, its temperature rises and thermal gradients appear, taking a shape that depends also on the cooling geometry. Edge-cooling of a laser rod[26] induces radial gradients, whereas cooling through the optical faces like in laser thin-disks[27] produces mostly longitudinal gradients. Optical wavefront distortion due to the variation of refractive index with temperature degrades the laser beam quality, and stress-induced birefringence due to inhomogeneous thermal expansion distorts its polarisation locally. Contrarily to laser amplification, frequency conversion in birefringent quadratic nonlinear crystals does not involve as strong heat deposition within the optical medium. However, this process is usually far more sensitive to refractive-index inhomogeneities induced by the thermal load, since a typical variation of the fourth decimal of the refractive index over typical centimetric distances alters phase-matching and ruins conversion efficiency. High static birefringence is needed to compensate for chromatic dispersion and achieve phase-matching, especially in the ultraviolet. It generally outweighs stress-induced birefringence by several orders of magnitude. Except in particular directions out-of-principal planes, polarisation state is not impaired by thermal stress, but frequency conversion is, since stress-optic effects contribute to the refractive index change locally by the same order of magnitude as thermo-optic effects. LBO being pyroelectric, transient temperature

gradients induce inhomogeneous charge migrations with their own anisotropic dynamics, ionic conductivity being highly direction-dependent. Thermally-induced inhomogeneous electric fields within the material not only contribute to mechanical stress through the reverse piezo-electric effect but also to additional transient, inhomogeneous, and anisotropic refractive index perturbations due to the Pockels electro-optics tensor. Thermal, stress-optic, and pyroelectric effects do not only degrade the generated beam quality, but impact the core of the generation process itself.

3.1 Original Cooling Arrangement

Several approches have been proposed and demonstrated to minimize temperature gradients. Surface cooling by a homogeneous broad laminar gas flow of large nonlinear optical crystals was proposed in 1987 by Eimerl.[28] This technique has been successfully applied to a number of large aperture, high-power laser amplifiers[29,30] and proposed for frequency converters.[31] Cryogenic helium gas is usually chosen due to its superior heat capacity. Optical contacting or bonding LBO to higher thermal conductivity optical materials such as sapphire[32] or diamond faces technical difficulties in such large transverse dimensions. Large thermal expansion difference, resistance of the bonding interface to optical damage at high intensity and high average-power in the ultraviolet are likely to be an issue *per se*.

We propose here a novel approach. A tightly localised gas flow removes heat directly on the LBO optical surfaces as close as possible to where it was deposited. To first order, thermal exchange is proportional to the temperature difference between the gas flow and the solid surface. Crystal edges were therefore thermalised to elevated temperature in order to improve heat extraction. In addition, since the thermal load is expected to be small in our case, we opted for simple forced-air cooling, at an air flow temperature slightly below room temperature.

As confirmed by transient thermal simulations with Cast3M finite-element numerical code,[33] cooling homogeneously over a spot half the Gaussian beam diameter, makes it possible to flatten the transverse temperature gradient to negligible values. Figure 4 shows that setting the crystal temperature to 100-120°C and cooling on a *single-face* through a continuous localised air-flow at 15°C is enough to compensate for a 4 W absorbed power at 1 kHz. Conservative exchange coefficients were used. Optimising convective heat transfer,[34] and cooling both optical surfaces, would improve heat extraction performance.

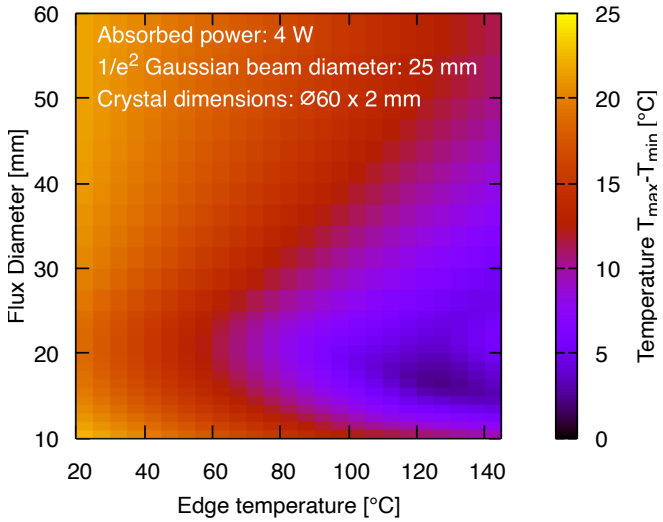

Figure 4. Simple simulation of the performances of localised air-flow cooling on the output-face of the quadrupler. The maximum temperature difference $T_{max} - T_{min}$ across the input Gaussian beam $1/e^2$ diameter is plotted in false colors as a function of crystal edge temperature (horizontal) and diameter of the cooled area (vertical). A heat-transfert coefficient of $10\,\mathrm{W/m^2/K}$ was applied for natural convection with regard to ambiant air at 22°C on the input surface. A heat-transfert coefficient of $60\,\mathrm{W/m^2/K}$ was applied for forced-air at 15°C on the output surface.

3.2 Forced-air Surface Cooling

Rapid deep-UV aging of LBO in our demanding high-intensity conditions was initially more of a concern* than optimising cooling. Due to experimental schedule constraints, it was chosen to rely on a commercial portable air-conditionner (Electrolux model EXP34U338HW, rated at 360 m^3/h) operating at maximum power to provide for cool air flux. Temperature was permanently set to minimum (16^{o}C) on the control panel. Unfiltered ambiant air from the laboratory was blown at maximum fan speed on the quadrupler output surface through a flexible PVC air duct terminated by linearly converging metal nozzles of various shapes. In normal operation, the compressor of this air conditionner starts and stops every 10 minutes, modulating output temperature between 3^{o}C and 15^{o}C with a 20-minute period at the center of the air duct before the nozzle. Air speed was measured at 11 m/s with a anemometer at this position. Turbulent air-flow at the output of the nozzle was not characterised. Temperature fluctuations were certainly of reduced amplitude according to thermocouple measurements. Under permanent operation, the generated UV energy fluctuate according to the air conditionner cycles. Air-flow cooling is currently being upgraded as far as surface contamination and aerodynamics are concerned.

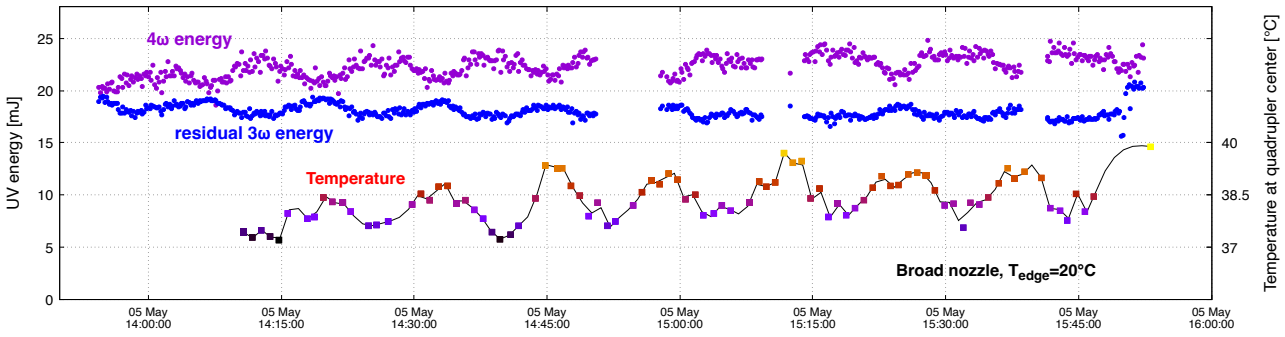

Figure 5. Correlation between the temperature at the center of the quadrupler crystal, measured through remote infrared thermography, and output energies in the UV. Both closely follows the cycles of the air conditionner. Quadrupler edges are thermalised at room temperature, and a broad nozzle blows air over a large area. This inefficient configuation is particularly sensitive to the temperature fluctuations of the gas flow. Setting the crystal to higher temperature and reducing the cooled area decrease sensitivity and improves performance.

3.3 Edge Thermalisation

Designing thermalised mounts for large crystals required special care due to the unusually strong and anisotropic thermal expansion of LBO.[35] Crystals are maintained in metallic frames that are positioned at the center of motor-controlled gimbals. Frames for circular crystals were manufactured in stainless steel by laser powder-bed fusion additive manufacturing, followed by fine surface finishing on the lathe. A semi-circular hollow channel was buried within the inner elastic ring (fig. 6). It allows for a liquid coolant to circulate as close as 400 μm from crystal edges. This makes it possible to uniformly ($\pm 0.5^o$C) set edge temperature between 15^{o}C and 55^{o}C on the full perimeter, according to direct contact and remote infrared thermographic characterisation. Due to anisotropic thermal expansion in LBO, dimensions shrink along Y optical axis, while they expand along X and Z axes as temperature rises. Whereas positive differential expansion (up to 56 μm) with regard to the metal frame are easily compensated for by two 100 μm indium interface layers, negative differential thermal expansion (up to 135 μm) would create an air gap, loosing thermal contact. The frame includes one mobile part that adapts to crystal dimensions. It loosely slides along the shrinking axis but is permanently maintained in contact to the crystal thanks to springs. The other half is fixed through thermally isolating plastic spacers on the gimbal assembly. Crystals are held in shallow grooves, slightly broader that crystal thickness, allowing for stress-free longitudinal differential thermal expansion permitted by soft and ductile indium interfaces. Permanent good thermal contact all around the crystals and absence of anomalous stress-induced refractive index changes were checked through Mach-Zehnder interferometry and infrared thermography, while slowly cycling temperatures multiple times. The

*That proved to be unfounded, at least up to $\approx$ 50-hour intermittent operation at full 220 W input power at 1030 nm and output power of the order of 40 W at 257 nm.

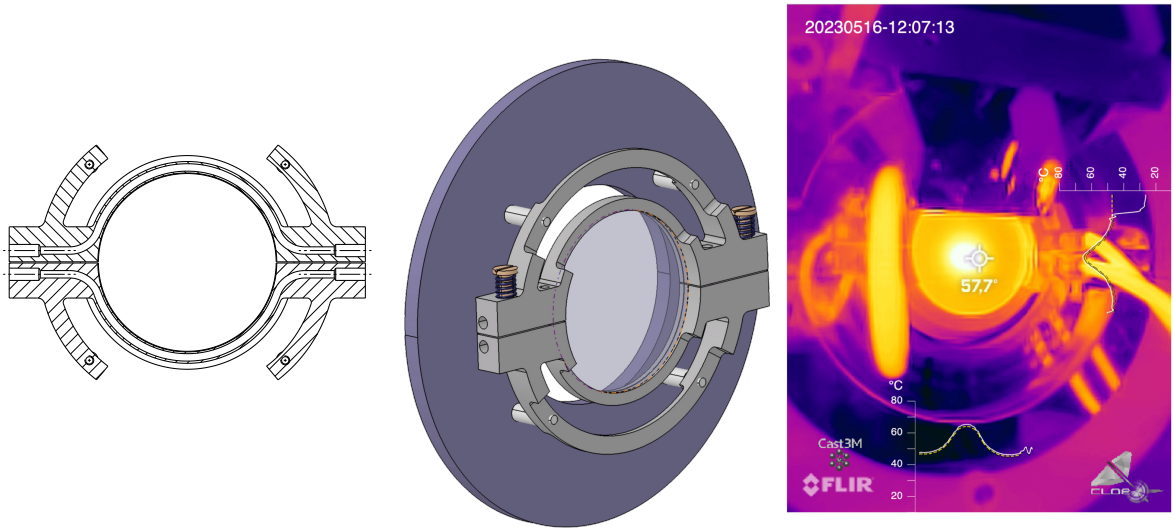

Figure 6. A hot liquid heat exchanger circulates in buried channels all around the crystals (left) in flexible thermal-expansion compensating metallic frames (center) to thermalise the crystals at elevated temperature (right) in order to facilitate surface gas flux heat extraction.

deviation of a HeNe laser pencil beam reflected on crystal surfaces was measured experimentally on the final assembly. It can be attributed to crystal anisotropic thermal expansion only, as predicted by thermo-mechanical simulations.[33]

4. EXPERIMENTAL SETUP

A dedicated bench, sketched in fig. 7, was appended to the laser system[36] developed for the Laser Lightning Rod Project[37] in order to characterise high-energy, high-power harmonic generation. The front-end of the laser system consists of a commercial fiber-based laser (Trumpf TruMicro 2000), providing 1 ns stretched pulses at 1030 nm. It seeds a commercial regenerative amplifier (Trumpf DIRA 200-1), operating at 1 kHz, that boosts the pulse energy up to 240 mJ. For the proof-of-concept deep-UV generation experiments reported below, the custom-design multipass amplifier capable of 800 mJ (in 4 multipass amplifying disks configuration) was bypassed. The beam was therefore sent directly to the Treacy compressor,[38] which was set to recompress the pulses slightly under 1 ps FWHM duration. Two parameters of the input beam were independently varied: pulse energy and duration. Energy was ramped up from 0 to 220 mJ thanks to a variable waveplate-polariser attenuator at the output of the regenerative amplifier. The front-end stretcher was tuned to vary the duration of the output pulses in the 1 ps to 15 ps range with either positive or negative ϕ_2 chirp.

Polarisation of the laser beam at fundamental frequency (1ω) onto the frequency conversion crystals (top-left in fig. 7, red) was vertical. Principal optical planes of all three frequency conversion crystals were horizontal (fig. 1). All three frequency conversion crystals were centered on large 200 mm gimbals mounts (Micro-Contrôle SL20A) computer-controlled through 1μm step-motor actuators for fine angular adjustments (10 μrad steps) about horizontal and vertical axes. Each of them is attached on large rotation stages (Micro-Contrôle RT120) that provide larger rotation about the vertical axis for rapid phase-matching tuning (170 μrad steps) as crystals heat-up due to absorption.

Laser beams are attenuated thanks to two specular reflections at 45^o incidence on UV-grade fused silica in the horizontal plan and vertical plane respectively, providing therefore similar attenuation regardless of polarisation. First reflection on the front surface of 10 cm thick slab[39] provides stronger attenuation for horizontally-polarised harmonics at 2ω and 4ω. The altitude of the beams over the bench is lowered thanks to a periscope made of a fused-silica wedged plate (top) followed by a aluminium-coated zerodur mirror (bottom). Uncoated input surface of the wedged plate conversely provides a stronger attenuation for vertically-polarised harmonics at 1ω and 3ω. A second 3-inch aluminum mirror folds the beam path towards a beam-reduction telescope, made of two uncoated

UV fused-silica positive lenses of 500 mm and 75.6 mm respectively. A first beam-splitter directs the reduced beam at 4ω towards a set of laser beam diagnostics (violet area in fig 7). A joulemeter (label G) measures the generated pulse-to-pulse UV energy. Three additional specular reflections on small fused-silica wedged plates further attenuate the beam for near-field measurements. A 250 mm AR-coated fused-silica lens is inserted along the path to image a plane 20 cm downstream of the quadrupler, on the window-less CMOS UV-enhanced sensor (2048×2048 12-bit, model GSENSE2020BSI, label E) without any optical density or spectral filters that would induce unpredictable and non-reproducible non-linear response and transmission loss. The same diagnostics are implemented for the harmonics at 3ω (blue area), 2ω (green area), and 1ω (red area). Imaging the same plane in the near field rely on window-less firewire 12-bit CCD A102f Basler cameras (labels A), without any optical density or filter. All cameras are externally triggered at 10 Hz and acquire beam profiles for the same pulse. Laser pulses at all four harmonics are continuously diagnosed in energy thanks to NIST-calibrated QE8SP-B-MT-D0 Gentec joulemeters (labels G) and Gentec Maestro energy monitors, externally triggered at the nominal 1 kHz repetition rate of the laser system.

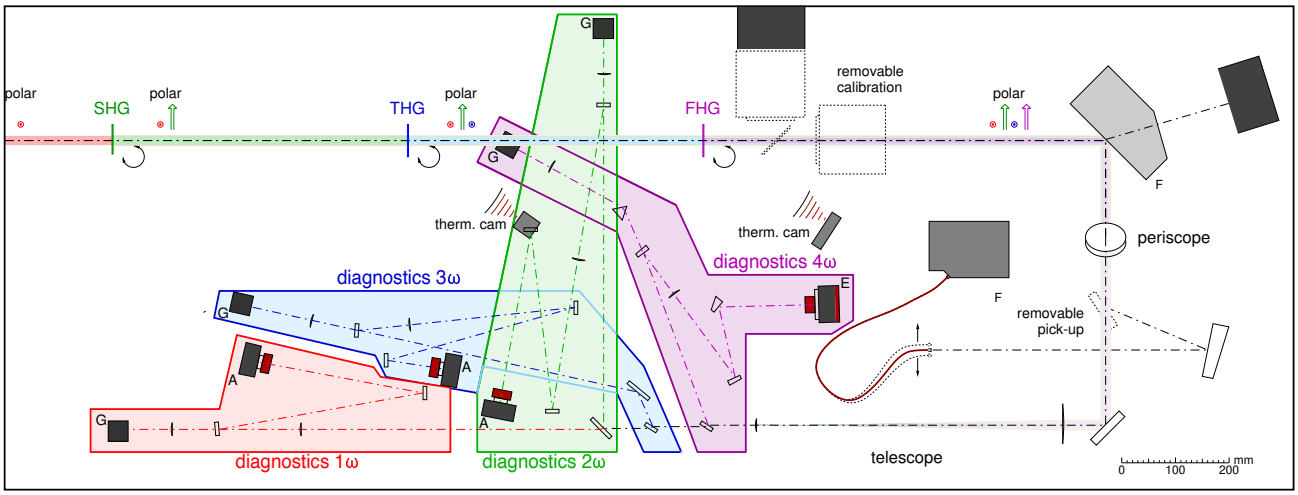

Figure 7. Layout of the frequency conversion bench. Fundamental beam (top left)

5. EXPERIMENTAL OPTIMISATION OF PULSE DURATION AND DOUBLER ANGULAR DETUNING

Optimum phase-matching angles were determined at low energy for each stage as a function of frame temperature. A systematic three parameter exploration of optimum angular detuning of the doubler, tripler and quadrupler was performed at four discrete energies of the laser system (60 mJ, 120 mJ, 180 mJ, and 220 mJ) and for various pulses durations in the 1 ps to 12 ps range. It confirmed the preliminary simulations above that the trippler was best set to zero phase-mismatch angle in all cases. Infrared thermographic monitoring did no exhibit any significant heating of the doubler due to nonlinear absorption. At full 220 W input power, and for a 9 ps stretched pulse duration, the maximum temperature increase at the center of the tripler was 5.2°C, which required a slight angular detuning compared to low power settings. Optimum pulse stretch and doubler angular detuning were simultaneously determined as shown on fig 8 for maximum pulse energy. Crystal edge was set to elevated 55°C temperature but air-flow cooling was turned off. These measurements are obviously obtained in a transient-temperature regime in the quadrupler. Special care was paid to start each angular sweep of the doubler in the same initial thermal state, and proceed at the same speed for all recordings. Automated quick (120 s) and reproducible step-motor angular rotation and synchronised acquisitions were key to the success of this systematic exploration. As predicted by numerical simulations again, the optimum pulse duration corresponds to a negative pulse chirp, with a 10% increase of output energy in the deep UV compared to positive chirp. Its optimum value of 9 ps is 50% larger than predicted which might reflect a different balance of linear, quadratic and higher order non-linear effects. Optimum power in this transient-regime is above 42.5 W, which is remarkable and promising.

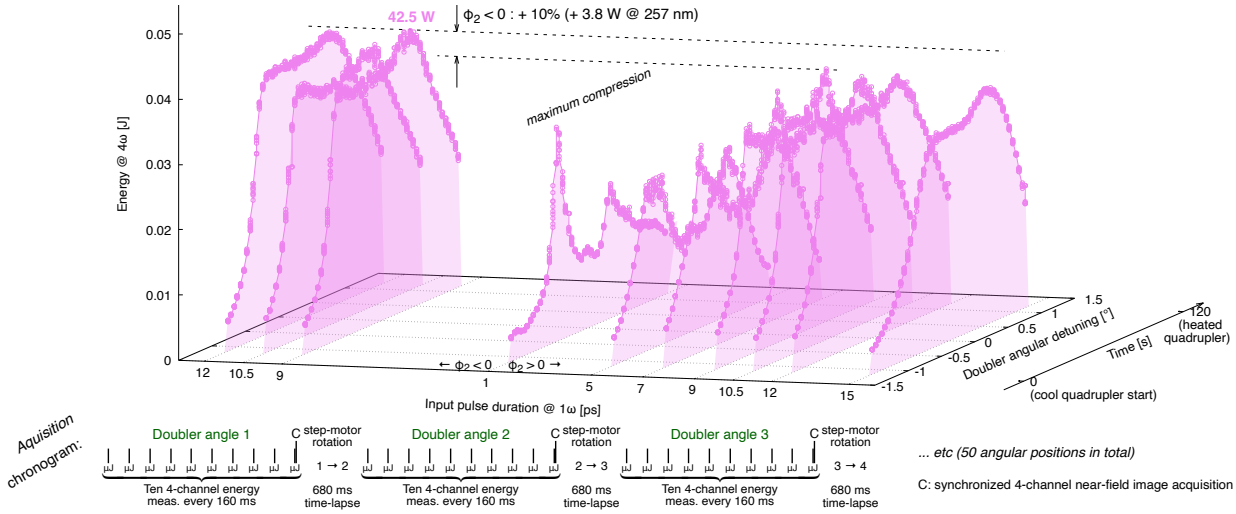

Figure 8. Experimental simultaneous optimisation of pulse duration and doubler angular detuning

6. STABILISATION OF DEEP-UV OUTPUT POWER THROUGH QUADRUPLER ANGULAR DETUNING

System parameters being optimised upstream, it was relatively easy to experimentally determine a quadrupler angular orientation that would stabilize UV output power. A cold-start in a phase-matched quadrupler reproduced the peak power of 42.5 W observed during the doubler optimisation process (fig. 9). Slowly retuning the quadrupler phase-matching angle to compensate for thermal drift, made it possible to recover up to 40 W at 257 nm, the small difference being attributed to temperature inhomogeneity. Figure 10 shows that the same crystal was still capable of producing 45 W, minimum, in the transient regime, after 50 hours of operation at high performance, although anti-reflection coatings were totally peeled-off under the beam footprint due to the combined effect of strong thermal stress induced by agressive cooling and high UV intensity.

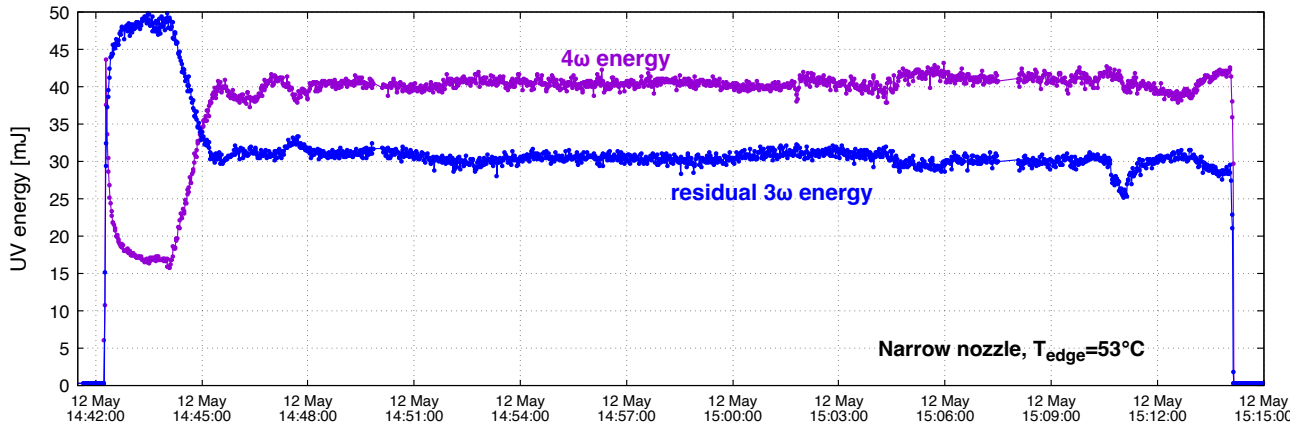

Figure 9. Cold-start and progressive quadrupler angular retuning made it possible to stabilise UV-output power to 40 W

7. EFFECTIVENESS OF THE SURFACE COOLING METHOD

Thermal exchange parameters were first fitted to infrared thermographic imaging measurements in a variety of situations (air-flow on/off, compressor on/off, various edge temperatures), which in absence of laser radiation made it possible to deduce a rough estimation of the absorbed power. Dirichlet conditions were applied on edge, with a time-dependent uniform temperature over the full perimeter $T_{\text{edge}}(t)$. Neumann conditions on optical

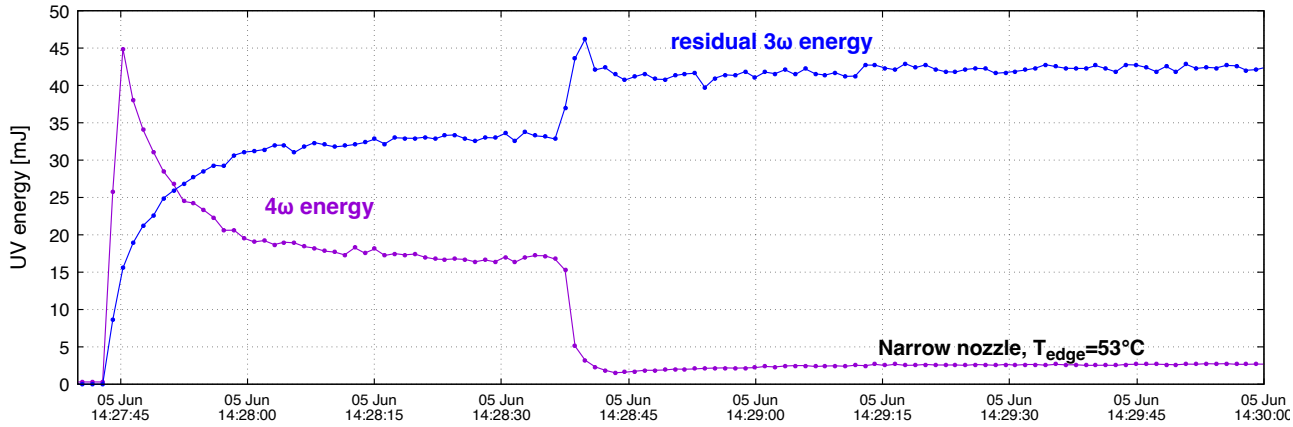

Figure 10. Transient deep-UV output power of 45 W, minimum. Actual peak transient performance might not even have been captured, since only one out of 1000 pulses were recorded.

surfaces, take the form of a separable Newton law $\Phi(x, y, t) = h(x, y)(T_p - T_\infty(t))$, combining a space-dependent convection exchange coefficient $h(x, y)$ in $\mathrm{W/m^2/K}$ reflecting inhomogeneous air-flow, and a time-dependent flux temperature $T_\infty(t)$, accounting for compressor cycling. An emissivity $\varepsilon = 0.95$ was assumed. Anisotropic, and temperature-dependent thermal conductivity was taken into account.[35] Although the procedure made it possible to fit the temperature at center (fig. 11) in this variety of conditions, estimation of the space-dependent convective exchange coefficient and the time-dependent air temperature at the nozzle output were not deemed reliable enough to deduce the absorbed power from measurements under air-flow cooling. The estimation below is based on simpler natural convection. The effectiveness of our cooling method is illustrated on figure 12. The beam near-field profiles at all four harmonics are plotted in shaded colors. As above, the selected metric was the maximum temperature difference over the $1/e^2$ input beam cross-section, materialised by vertical dashed lines. Temperature distribution on the quadrupler output surface was recorded by infrared thermographic imaging. Vertical temperature profiles are truncated on the left-hand side by the metallic nozzle. They are more symmetric in the horizontal direction, perpendicular to the air-flow. Top temperature profiles (in red) correspond to a transient-temperature regime where air-flow cooling is off. Temperature at center was above 65^{o}C. Generated power was of the order of 45 W but it was necessary to correct the quadrupler angular orientation to compensate for phase-matching thermal drift. The typical temperature difference was in this case of the order of 7.2^{o}C. Dashed lines correspond to Cast3M simulations with an total absorbed power of 1.1 W.

The bottom curves (blue color) correspond to air-flow cooled surface and a cold edge, at room temperature. Air flow from top to bottom which explains the asymmetry in the vertical profile. The temperature difference - above 20^{o}C - results in less efficient deep-UV conversion, of the order of 28 W, but *stabilised*. Heating the edge (brown curve) results in a smaller temperature difference - here between 16.4 and 17.8^{o}C - which is in qualitative

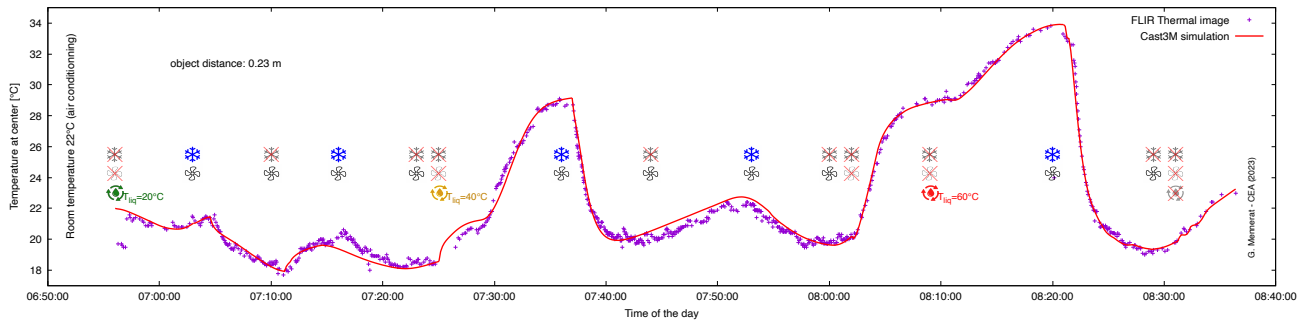

Figure 11. Fitting parameters of the thermal model for the finite-element simulation provided the thermal exchange factors for conduction on edge and convection on surfaces

agreement with simulations. A much smaller nozzle would be required to avoid cooling an area larger than the beam itself and further minimise the temperature gradient. Deep-UV power has been consistently stabilised close to 40 W for several days over the course of measuring spatially resolved spectra at all four wavelengths, with a nozzle brought even closer to the surface.

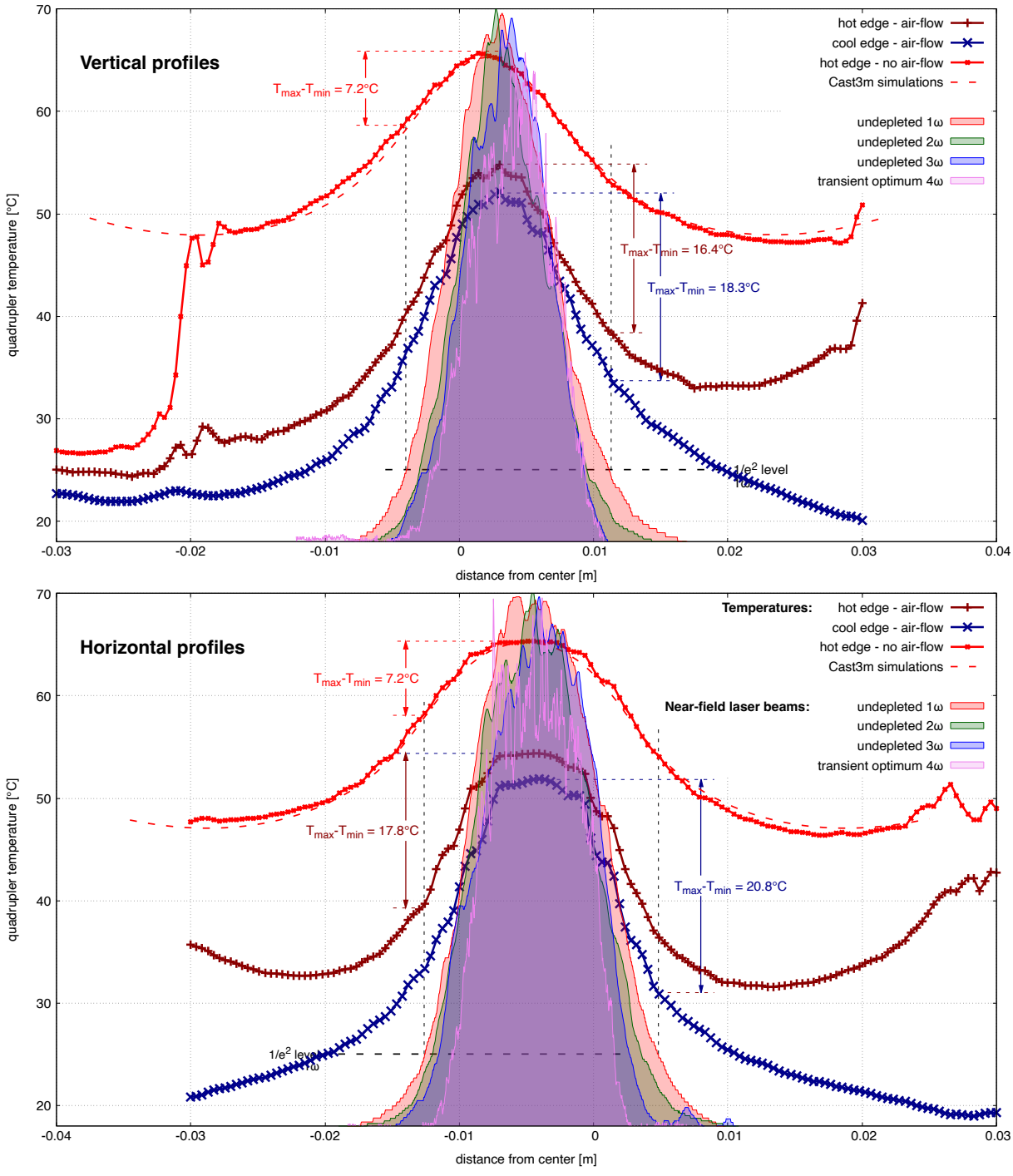

Figure 12. Measurements of temperature gradients in various conditions

8. BEAM PROFILES

Beam profiles were systematically recorded at 10 Hz alongside energy measurements. Best profiles are presented on figure 13. Fluence profiles at 2ω and 4ω seem to exhibit small-scale orange-peel like shot-to-shot fluctuations that may be the signature of optical Kerr-effect, possibly including $\chi^{(2)}$ cascading. Small-scale fluctuations are less apparent at 1ω and 3ω, but Kerr coefficients differ since these waves are polarised in other planes. Due

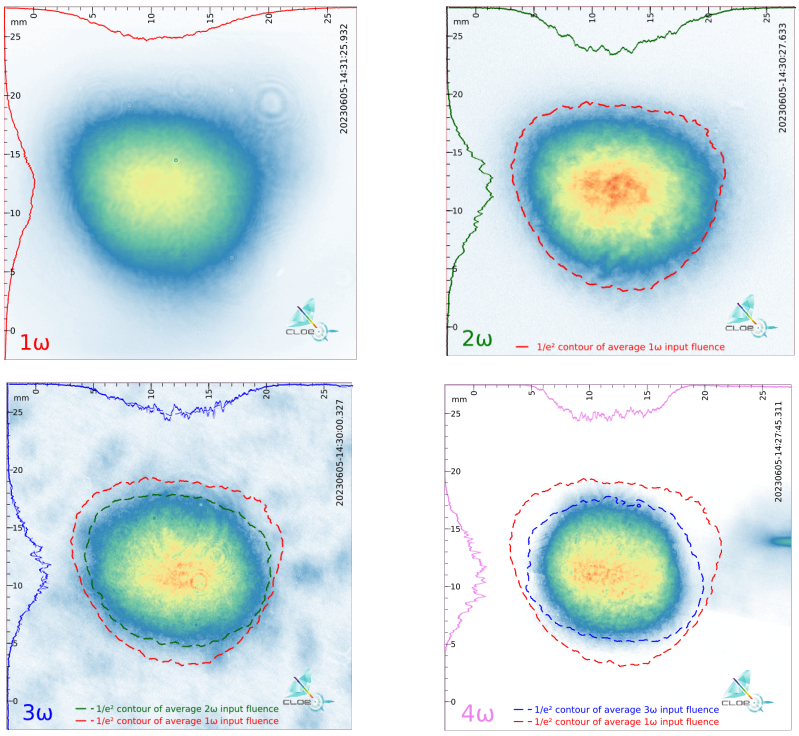

Figure 13. Typical near-field fluence profiles of un-depleted 1ω, 2ω, and 3ω beams, as well as transient 4ω beam in absence of air-flow cooling, all measured through imaging a plane 20 cm downstream from quadrupler output

to imperfect cooling and residual temperature gradients, power stabilisation of fig. 9 was only possible at the expense of beam homogeneity. Corresponding typical output beam profiles are shown in fig. 14. The origin of the anisotropy of these typical and reproducible beam profiles is currently under investigation.

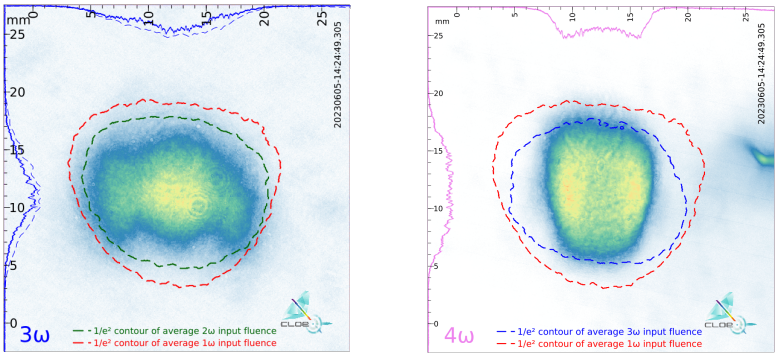

Figure 14. Typical near-field fluence profiles in the ultraviolet, in thermal steady-state situations, showing the effect of inhomogeneous temperature gradients

9. CONCLUSION

To the best of our knowledge, 40-45 W average powers measured here at 257 nm are the highest ever produced in an all-solid-state laser system at high energy in this wavelength region. Intermittent operation over 50 hours in the course of two months did not exhibit any internal damage or performance degradation. Proof of concept for a novel surface cooling method has been demonstrated and is promising. Enhancements to the preliminary air cooling system of our first prototype are currently being implemented. Air flow does not induce any measurable pointing instability. Closed-loop angular phase-matching tuning to compensate for quadrupler thermal drift is not necessary. Spatially-resolved spectra were also recorded at 1, 2, 3, and 4ω. They will help elucidate the beam shape at 4ω in presence of thermal gradients, combined with thermo-optical and thermo-elasto optical finite-element simulations. Ramping up to higher power is possible.

ACKNOWLEDGMENTS

This work was partially funded by from the ANR through the LabCom program under the grant agreement ANR-20-LCV1-0004-001, as well as European Union Horizon 2020 Research and innovation program FET–OPEN under the grant agreement no 737033-LLR.

We acknowledge Sylvain Foucquart, André Fillon, Dominique Porterat, Olivier Hercher, Hicham Maskrot, Olivier Gobert, and Delphine Guillaumet from CEA Saclay, as well as Victor Moreno from the University of Geneva for their contributions to the experimental setup.

REFERENCES

[1] Houard, A., Walch, P., Produit, T., Moreno, V., Mahieu, B., Sunjerga, A., Herkommer, C., Mostajabi, A., Andral, U., André, Y.-B., Lozano, M., Bizet, L., Schroeder, M. C., Schimmel, G., Moret, M., Stanley, M., Rison, W. A., Maurice, O., Esmiller, B., Michel, K., Haas, W., Metzger, T., Rubinstein, M., Rachidi, F., Cooray, V., Mysyrowicz, A., Kasparian, J., and Wolf, J.-P., "Laser-guided lightning," *Nature Photonics* **17**(3), 231–235 (2023).

[2] Andral, U., Walch, P., Moreno, V., Mahieu, B., Produit, T., Lozano, M., Bizet, L., Herkommer, C., Moret, M., André, Y.-B., Krötz, P., Metzger, T., Michel, K., Mysyrowicz, A., Kasparian, J., Lupinski, D., Houard, A., and Wolf, J.-P., "Second and third harmonic generation from simultaneous high peak- and high average-power thin disk laser," *Applied Physics B* **128**, 177 (Aug 2022).

[3] Balitski, D., Villeval, P., and Lupinski, D., "Recent progress on large aperture LBO and RTP optics for efficient harmonics generation and high power lasers," in [*Optica Advanced Photonics Congress 2022*], AM6A.3, Optica Publishing Group (2022).

[4] Kokh, A., Kononova, N., Mennerat, G., Villeval, P., Durst, S., Lupinski, D., Vlezko, V., and Kokh, K., "Growth of high quality large size LBO crystals for high energy second harmonic generation," *Journal of Crystal Growth* **312**(10), 1774–1778 (2010).

[5] Mennerat, G., Bonville, O., Garrec, B. L., Villeval, P., Durst, S., Lupinski, D., Kokh, A., Kononova, N., Vlezko, V., and Kokh, K., "Frequency doubling and tripling for future fusion drivers," in [*Nonlinear Optics*], NThA2, Optica Publishing Group (2011).

[6] Yang, S. T., Henesian, M. A., Weiland, T. L., Vickers, J. L., Luthi, R. L., Bielecki, J. P., and Wegner, P. J., "Noncritically phase-matched fourth harmonic generation of Nd:glass lasers in partially deuterated KDP crystals," *Opt. Lett.* **36**, 1824–1826 (May 2011).

[7] Délen, X., Deyra, L., Benoit, A., Hanna, M., Balembois, F., Cocquelin, B., Sangla, D., Salin, F., Didierjean, J., and Georges, P., "Hybrid master oscillator power amplifier high-power narrow-linewidth nanosecond laser source at 257 nm," *Opt. Lett.* **38**, 995–997 (Mar 2013).

[8] Orii, Y., Yoshii, K., Kohno, K., Tanaka, H., Shibuya, K., Okada, G., Mori, Y., Nishimae, J., and Yoshimura, M., "High-power deep-ultraviolet light generation at 266 nm from frequency quadrupling of a picosecond pulsed 1064 nm laser with a Nd:YVO_4 amplifier pumped by a 914 nm laser diode," *Opt. Express* **31**, 14705–14714 (Apr 2023).

[9] Mennerat, G., Farcage, D., Mangote, B., Villeval, P., and Lupinski, D., "High-efficiency, high-power frequency quadrupling to 266 nm in LBO," in [*Advanced Solid State Lasers*], ATh2A.42, Optica Publishing Group (2014).

[10] Wang, N., Zhang, J., Yu, H., Lin, X., and Yang, G., "Sum-frequency generation of 133 mJ, 270 ps laser pulses at 266 nm in LBO crystals," *Opt. Express* **30**, 5700–5708 (Feb 2022).

[11] Fu, S., Mahieu, B., Mysyrowicz, A., and Houard, A., "Femtosecond filamentation of optical vortices for the generation of optical air waveguides," *Opt. Lett.* **47**, 5228–5231 (Oct 2022).

[12] Walch, P., Mahieu, B., Moreno, V., Produit, T., Andral, U., André, Y.-B., Bizet, L., Lozano, M., Herkommer, C., Moret, M., Jung, R., Bessing, R., Klingebiel, S., Bertho, Y., Metzger, T., Mysyrowicz, A., Wolf, J.-P., Kasparian, J., and Houard, A., "Long distance laser filamentation using Yb:YAG kHz laser," *Scientific Reports* **13**(1), 18542 (2023).

[13] Smith, A. V. and Bowers, M. S., "Phase distortions in sum- and difference-frequency mixing in crystals," *J. Opt. Soc. Am. B* **12**, 49–57 (Jan 1995).

[14] Smith, A. V., Gehr, R. J., and Bowers, M. S., "Numerical models of broad-bandwidth nanosecond optical parametric oscillators," *J. Opt. Soc. Am. B* **16**, 609–619 (Apr 1999).

[15] *SNLO nonlinear optics code available from A. V. Smith, AS-Photonics, Albuquerque, NM* (version 79, 2023).

[16] Kato, K., "Temperature-tuned 90^o phase-matching properties of LiB_3O_5," *IEEE Journal of Quantum Electronics* **30**(12), 2950–2952 (1994).

[17] Miller, R. C., "Optical Second Harmonic Generation in Piezoelectric Crystals," *Applied Physics Letters* **5**, 17–19 (11 2004).

[18] Garrett, C. and Robinson, F., "Miller's phenomenological rule for computing nonlinear susceptibilities," *IEEE Journal of Quantum Electronics* **2**(8), 328–329 (1966).

[19] Alford, W. J. and Smith, A. V., "Wavelength variation of the second-order nonlinear coefficients of $KNbO_3$, $KTiOPO_4$, $KTiOAsO_4$, $LiNbO_3$, $LiIO_3$, β-BaB_2O_4, KH_2PO_4, and LiB_3O_5 crystals: a test of Miller wavelength scaling," *J. Opt. Soc. Am. B* **18**, 524–533 (Apr 2001).

[20] Flytzanis, C., "2 - Theory of Nonlinear Optical Susceptibilities," in [*Quantum Electronics: A Treatise. Volume I: Nonlinear Optics, Part A*], Rabin, H. and Tang, C., eds., 9–207, Academic Press (1975).

[21] Li, H., Kam, C., Lam, Y., and Ji, W., "Femtosecond Z-scan measurements of nonlinear refraction in nonlinear optical crystals," *Optical Materials* **15**(4), 237–242 (2001).

[22] Maingot, B., Neradovskaia, E., Claudet, C., Forget, N., and Jullien, A., "Measurement of nonlinear refractive indices of bulk and liquid crystals by nonlinear chirped interferometry," *Opt. Lett.* **48**, 3243–3246 (Jun 2023).

[23] Röcker, C., Weinert, P., Villeval, P., Lupinski, D., Delaigue, M., Hönninger, C., Weber, R., Graf, T., and Abdou Ahmed, M., "Nonlinear absorption in lithium triborate frequency converters for high-power ultrafast lasers," in [*Optica Advanced Photonics Congress 2022*], AM6A.5, Optica Publishing Group (2022).

[24] Röcker, C., Weinert, P., Villeval, P., Lupinski, D., Delaigue, M., Hönninger, C., Weber, R., Graf, T., and Abdou Ahmed, M., "Nonlinear absorption in lithium triborate frequency converters for high-power ultrafast lasers," *Opt. Express* **30**, 5423–5438 (Feb 2022).

[25] Mennerat, G., "High performance materials and new approaches for frequency conversion to UV and DUV at high energy," in [*Optica Advanced Photonics Congress 2022*], AM6A.1, Optica Publishing Group (2022).

[26] Levine, A. K., ed., [*Lasers - A series of advances*], vol. 2, Marcel Dekker, New-York (1968).

[27] Giesen, A., Hügel, H., Voss, A., Wittig, K., Brauch, U., and Opower, H., "Scalable concept for diode-pumped high-power solid-state lasers," *Applied Physics B* **58**(5), 365–372 (1994).

[28] Eimerl, D., "High average power harmonic generation," *IEEE Journal of Quantum Electronics* **23**, 575–592 (May 1987).

[29] Divoký, M., Pilař, J., Hanuš, M., Navrátil, P., Denk, O., Severová, P., Mason, P., Butcher, T., Banerjee, S., Vido, M. D., Edwards, C., Collier, J., Smrž, M., and Mocek, T., "150 J DPSSL operating at 1.5 kW level," *Opt. Lett.* **46**, 5771–5773 (Nov 2021).

[30] Divoky, M., Phillips, J., Pilar, J., Hanus, M., Navratil, P., Denk, O., Paliesek, T., Severova, P., Clarke, D., Smrz, M., and et al., "Kilowatt-class high-energy frequency conversion to 95 J at 10 Hz at 515 nm," *High Power Laser Science and Engineering* **11**, e65 (2023).

[31] Bayramian, A., Henesian, M., and Bullington, A., "High average power frequency conversion," in [*7th International High Energy Class Diode Pumped Solid State Lasers (HEC-DPSSL) Workshop*], (dec 2012).

[32] Rothhardt, C., Rothhardt, J., Klenke, A., Peschel, T., Eberhardt, R., Limpert, J., and Tünnermann, A., "BBO-sapphire sandwich structure for frequency conversion of high power lasers," *Opt. Mater. Express* **4**, 1092–1103 (May 2014).

[33] *Cast3M: finite element code*. developed by CEA http://www-cast3m.cea.fr (2023).

[34] Sun, F., Sun, D., Ren, F., Fu, G., Wang, K., and Zhang, Z., "Impact of forced convective heat transfer on temperature uniformity and frequency doubling efficiency in large aperture ammonium dihydrogen phosphate (ADP) crystals," *Optics & Laser Technology* **171**, 110348 (2024).

[35] Grechin, S. G., Zuev, A. V., Kokh, A. E., Moiseev, N. V., Popov, P. A., Sidorov, A. A., and Fokin, A. S., "Thermophysical parameters of the LBO crystal," *Quantum Electronics* **40**(6), 509 (2010).

[36] Herkommer, C., Krötz, P., Jung, R., Klingebiel, S., Wandt, C., Bessing, R., Walch, P., Produit, T., Michel, K., Bauer, D., Kienberger, R., and Metzger, T., "Ultrafast thin-disk multipass amplifier with 720 mJ operating at kilohertz repetition rate for applications in atmospheric research," *Opt. Express* **28**, 30164–30173 (Sep 2020).

[37] Produit, T., Walch, P., Herkommer, C., Mostajabi, A., Moret, M., Andral, U., Sunjerga, A., Azadifar, M., André, Y.-B., Mahieu, B., Haas, W., Esmiller, B., Fournier, G., Krötz, P., Metzger, T., Michel, K., Mysyrowicz, A., Rubinstein, M., Rachidi, F., Kasparian, J., Wolf, J.-P., and Houard, A., "The laser lightning rod project," *Eur. Phys. J. Appl. Phys.* **93**, 10504 (Jan 2021).

[38] Treacy, E., "Optical pulse compression with diffraction gratings," *IEEE Journal of Quantum Electronics* **5**(9), 454–458 (1969).

[39] Journot, E., "Device for sampling a plurality of parts of a light beam," (U.S. Patent 8 120 863 B2, Feb. 2012).